Hierarchical modeling of mechano-chemical dynamics of epithelial sheets across cells and tissue

Yoshifumi Asakura[a], Yohei Kondo[b,c,d], Kazuhiro Aoki[b,c,d], Honda Naoki[a, e*]

[a] Laboratory for Theoretical Biology, Graduate School of Biostudies, Kyoto University, Sakyo, Kyoto, Kyoto 606-8315, Japan

[b] Quantitative Biology Research Group, Exploratory Research Center on Life and Living Systems (ExCELLS), National Institutes of Natural Sciences, 5-1 Higashiyama, Myodaiji-cho, Okazaki, Aichi 444-8787, Japan.

[c] Division of Quantitative Biology, National Institute for Basic Biology, National Institutes of Natural Sciences, 5-1 Higashiyama, Myodaiji-cho, Okazaki, Aichi 444-8787, Japan.

[d] Department of Basic Biology, School of Life Science, SOKENDAI (The Graduate University for Advanced Studies), 5-1 Higashiyama, Myodaiji-cho, Okazaki, Aichi 444-8787, Japan.

[e] Research Center for Dynamic Living Systems, Kyoto University, Sakyo, Kyoto, Kyoto 606-8315, Japan

Corresponding author: Honda Naoki
Address: Graduate School of Biostudies, Kyoto University, Yoshidakonoecho, Sakyo-ku, Kyoto, Kyoto 606-8315, Japan
Tel.: +81-75-753-4422
E-mail: honda.naoki.4v@kyoto-u.ac.jp

Keywords: mathematical model; continuum dynamics; ERK; wound healing

Competing Interests: The author has declared that no competing interests exist.

Abstract

Chemical and mechanical properties on a tissue regulate cellular migration. The orchestrated collective cell migration is a fundamental process in embryonic development and tissue homeostasis. Intra-cellular chemical signal network has been revealed by molecular biological researches, but there remains a fundamental question how the cell population level phenomenon is emerged across the hierarchy from the single-cell level process. However, there is a huge gap in our understanding between the microscopic single-cell behavior and macroscopic multicellular dynamics. To fill the hierarchical gap, we have focused on a wound healing experimental system in which ERK propagating wave from the wound edge mediates collective cell migration in the opposite direction. To reveal the mechanisms in which cellular dynamics causes tissue dynamics, here we proposed a hierarchical framework utilizing continuum dynamics formulation. Our continuum model recapitulated the cell migration observed in experiments to an opposite direction of ERK waves, and we confirmed a consistency with our previous single-cellular dynamics model. Here, our new model showed the mechanisms by which the collective tissue behavior emerges at the cell population level. Therefore, this approach allows us to seamlessly connect the hierarchical causality from single-cell level to tissue level.

Introduction

Collective cell migration in epithelial sheets plays an important role in embryonic development and tissue homeostasis (Friedl and Gilmour, 2009). How such a cell population level phenomenon is emerged across the hierarchy from the single-cell level process is a fundamental question for understanding multicellular system. However, there is a huge gap in our understanding between the microscopic single-cell behavior and macroscopic multicellular dynamics. To fill the gap, we need to understand how the cells are interacted**.** Cell surface molecules and secretory molecules have been reported to mediate cell-cell communication, but only such chemical signals have been focused. On the other hand, mechanical signals such as intercellular pressure or external force have been investigated just recently (Pascalis and Etienne-Manneville, 2017). Thus, how the cells integrate mechano-chemical signals remain elusive.

Recently, we showed that the collective cell migration during wound healing was mediated by mechano-chemical cellular dynamics *in vivo* and *in vitro* (Aoki et al., 2017; Hiratsuka et al., 2015). In these studies using a biosensor based on the principle of fluorescence resonance energy transfer (FRET), we live-imaged extracellular signal-related kinase (ERK) activity during wound healing, because ERK has been reported to regulate cell migration both *in vitro* and *vivo* (Huang et al., 2004; Kamioka et al., 2012; Komatsu et al., 2011; Mizuno et al., 2014). We then discovered that ERK activation spreaded in space and time as traveling waves across epithelial sheet and that cells collectively move in the opposite direction to ERK waves (Fig. 1). We also showed that cells changed their mobility and volume in response to the ERK activation. To understand how the ERK activation wave is transformed to collective cell migration, we previously developed a particle-based model of epithelial cell population (Aoki et al., 2017). This model was formulated as a one-dimensionally aligned particles connected through springs, in which particles and springs represent cells and elastic interaction, respectively. According to our experiments, we incorporated the effects of ERK signal on cellular mechanical properties in the model; ERK-dependent mobility and volume. Using the computer simulation, our model successfully recapitulated basic property of ERK-mediated collective cell migration, namely, cells migrate in the opposite direction to the ERK traveling wave.

However, there still remain problems; the particle-based model was incapable of comparing the experimental data with the theoretical model directly, because of the following discrepancies. First, regarding dimensions, our previous model was implemented in one-dimension, while the epithelial tissue migrated in two-dimensions. Second, even in a possible 2D model, it is hard to compare the model with cellular behaviors observed in live-imaging, due to plastic nature of the tissue; the tissue is not like solid in which cellular positions are stably fixed, but it behaves like fluid in which cellular positions are rearranged ever fluctuating in time and cells stochastically pass through others. Third, the heterogeneity of the cells is also problematic. Cellular responses are indeed heterogeneous, but our previous model assumed that cells are homogeneous with the same parameter values.

To overcome these aforementioned problems, we aimed to acquire a coarse-grained model of the two-dimensional epithelial dynamics that averages the heterogeneous individual cells. We thus proposed a new hierarchical approach, in which our particle-based model of the ERK-mediated collective cell migration was approximately translated into a continuum model. This approach allows seamlessly connecting hierarchical causality from single-cell level to tissue level. In the following sections, we describe the particle-based model and its transformation to continuum model, and then show the validity of our hierarchical approach by comparing these two models in numerical simulations.

Results

Particle-based model

Previously, we developed a particle-based model to understand how the ERK traveling wave-mediated collective cell migration in epithelial sheet, in which the cells adhere to neighboring cells so that the cells cannot freely migrate, but rather mechanically interacted each other through repulsive and attractive forces (Fig. 2A). In the model, the epithelial sheet was addressed as one-dimensional (1D) series of particles connecting through springs, where particles denote positions of cells and springs represents elastic property of the cells involved in membrane, cytoskeleton and adhesion. Thus, the dynamics of the cellular position xi are described by following ordinary differential equations (ODEs):

$$\frac{dx_i}{dt} = v_i \tag{1}$$

$$\frac{dv_i}{dt} = -\mu_i v_i - k[(R_{i+1} + R_i) - (x_{i+1} - x_i)] + k[(R_i + R_{i-1}) - (x_i - x_{i-1})] + \eta(v_{i+1} - v_i) - \eta(v_i - v_{i-1}), \tag{2}$$

where xi and vi indicate the position and the velocity of the *i*-th cell, respectively; k indicates spring constant of the cell; Ri and μi indicate cell radius and friction coefficient, respectively. We also modified the previous model by incorporating effect of intercellular viscosity in the fourth term (Aoki et al., 2017). Because cell size and mobility were upregulated by ERK activation in our previous report, we assumed that cell radius and friction were modulated by the ERK activity positively or negatively as

$$R_i = R_0(1 + \alpha ERK_i) \tag{3}$$

$$\mu_i = \mu_0 exp(-\beta ERK_i), \tag{4}$$

where Ro and mo indicate basal radius and basal friction of the cells, respectively; a and b denote effect of the ERK activity on cellular size and friction, respectively. ERKi denotes the ERK activity of the j-th cell as

$$ERK_j = A_0 exp\left(-\left(x_j - \left(x_{j,0} + ct\right)\right)^2 / 2\sigma^2\right), \tag{5}$$

where Ao, c and σ^2 indicate amplitude of ERK wave, velocity of ERK wave and a positive constant regulating width of the ERK wave, respectively.

Through the simulation, the modified model showed ERK-induced cell migration, in which the cells migrate towards the opposite direction to ERK travelling wave (Fig. 2B), consisting with our previous experiments. Additionally, by changing simulation parameters, opposite direction migration was abolished (Fig 2C, D).

Continuum model

We here coarse-grained the 1D particle-based model by continuum fluid dynamics approximation (Fig 3A). We first transformed equation (2) into

$$\frac{dv_j}{dt} = -\mu_j v_j - k\left(P_{j+1} - P_j\right) + \eta\left(v_{j+1} - 2v_j + v_{j-1}\right), \tag{6}$$

where $P_i=(R_i+R_{i-1})-(x_i+x_{i-1})$. P_i and P_{i+1} correspond to pressure from left and right neighboring cells, respectively. Since the cell density is number of cells within unit distance, $\rho_j = 1/\left(x_{j+1} - xj\right)$ and $\rho_j^\infty = 1/\left(R_{j+1}\left(ERK_{j+1}\right) - R_j\left(ERK_j\right)\right)$, so that

$$P_i = \frac{1}{\rho_i^\infty} - \frac{1}{\rho_i}. \tag{7}$$

To coarse-grain the equation (5), collective cell migration can be interpreted as a continuous flow field as below in Lagrangian description in fluid dynamics:

$$\frac{Dv}{Dt} = -\mu(ERK)v - k\frac{\partial P}{\partial x} + \eta\frac{\partial^2 v}{\partial x^2}, \tag{8}$$

where v indicates velocity of the flow field, $P = 1/\rho^{\infty} - 1/\rho$, and $D/Dt = \partial/\partial t + \mathbf{v}\ \mathbf{grad}$ (in this 1D case, $Dv/Dt = \partial v/\partial t + v\,\partial v/\partial x$). thus,

$$\frac{Dv}{Dt} = -\mu\exp(-\beta ERK)\,v - 2\alpha k R_0\frac{1}{\rho}\frac{\partial ERK}{\partial x} - \frac{k}{\rho^3}\frac{\partial\rho}{\partial x} + \frac{\eta}{\rho^2}\frac{\partial^2 v}{\partial x^2} - \frac{\eta}{\rho^3}\frac{\partial\rho}{\partial x}\frac{\partial v}{\partial x}. \tag{9}$$

Note that D/Dt is used for Lagrangian description in which velocity change is determined by tracking the motion of cells, whereas $\partial/\partial t$ is used for Eulerian description in which velocity change is written as a function of space and times.

In contrast to equation (5), v, P and ρ are not indexed by i, since we addressed these variables as continuous function in space and time. Cell density field also has a flux according to equation (7) and its dynamics is described by

$$\frac{D\rho}{Dt} = -\rho\frac{\partial v}{\partial x}. \tag{10}$$

ERK waves were given as the same function as those in particle based model (Fig 3B). With this continuum model, we performed simulations of fields of v and ρ in Euler description with ERK waves that travels into positive direction in x-axis. The resulting velocity field showed negative values (Fig 3C-E), indicating that there are flows into a direction opposite to the ERK waves. The opposite direction migration against ERK wave consists with our previous experiments. Consisting with the particle-based model, velocity fields showed the same direction values in some simulation parameters as shown in (Fig 3C-E).

Comparison between two models

Finally, to validate our continuum approximation, we compared simulation results generated by the two models. To do this, we numerically reconstructed trajectory of cellular migration, i.e., path line in fluid mechanics, from the simulated velocity field in continuum model (Fig 3C-E) (see Methods). It should be noticed that the velocity field in continuum model represents velocity at time t and space x, but does not correspond to tracking velocity of specific cells. By comparing the trajectories simulated in our two models, we confirmed that almost the same trajectories were generated by the two models in various parameters (Fig 4). It indicates that our fluid approximation is valid and the continuum model is able to explain ERK-dependent cell migration; cells migrate in opposite direction to traveling ERK waves across the tissues.

Discussion

We proposed hierarchical modeling approach for understanding of mechano-chemical epithelial dynamics, which acquires causality beyond the hierarchy between the levels of the cells and tissue. We presented that previous particle-based model at the level of cells can be hierarchically transformed into the continuum model for describing tissue-level epithelial dynamics. Through the numerical simulation, we demonstrated the clear consistency of the trajectories simulated by the continuum model and our previous particle model, showing the validity of our hierarchical modeling. Thus, our continuum model offers a new theoretical platform to integrate mechano-chemical signals that determine the cellular and tissue behaviors.

Previously, several coarse-grained models to describe the mechanical behavior of multicellular systems have been developed (Brodland, 2003; Fozard et al., 2009; Ishihara et al.; Murisic et al., 2015; Turner, 2005), however, there have been no models to incorporate the mechanical dynamics with molecular activities that quantitatively measured by recent imaging techniques with FRET-based biosensor. Because of this lack of integration, there have been a limited number of mechanistic insights into how intracellular signals, e.g., MAPK and WNT, regulate mechanical dynamics of the tissues and cells (Avvisato et al., 2007), in spite of recent progress of imaging techniques. Therefore, our model is the first coarse-grained model to integrate complex regulation of mechano-chemical tissue dynamics.

Although the epithelium tissue is a 2D sheet, our previous particle-based model was restricted in 1D. On the other hand, our continuum model can be easily extended to two-dimensional model. Thus, it reflects *in situ* 2D epithelial sheet dynamics observed by imaging experiments. Furthermore, because the continuum model coarse-grains noisy rearrangement of cells, our hierarchical modeling approach presents a new theoretical methodology to understand the tissue dynamics without monitoring all cellular behaviors. Therefore, the continuum model has advantages to interpret 2D epithelium sheet dynamics observed by the imaging data, compared with other cell-level models (cois Graner et al., 1992; Honda, 1983; Nonomura, 2012; Yamao et al., 2011).

Since recent progress in live cell imaging technique have increased the number of signaling molecules to monitor at once, future works need to determine importance of each factor. Our continuum model currently takes only one chemical factor, but extension with two or more factors are necessary. Along with the multiple-chemical signal quantifications, recent progress in quantitative biology field have enabled to measure mechanical signals such as pressure, density and so on. There were no methods, however, to analyze the mechanical signals with canonical molecular biochemical signals at the same time. Our continuum model provides a new theoretical basics to analyze the cellular system that integrate mechanical and chemical signals.

Methods

Detailed derivation of the continuum model

Equation (2) of the particle-based model is rewritten as

$$\frac{dv_i}{dt} = -\mu(ERK_i)v_i - k\left(x_{i+1/2} - x_{i-1/2}\right)\frac{P_{i+1/2} - P_{i-1/2}}{x_{i+1/2} - x_{i-1/2}} + \eta\left((x_{i+1} - x_i)\frac{v_{i+1} - v_i}{x_{i+1} - x_i} - (x_i - x_{i-1})\frac{v_i - v_{i-1}}{x_i - x_{i-1}}\right), \quad (11)$$

where $P_j = (R_{j+1/2} + R_{j-1/2}) - (x_{j+1/2} - x_{j-1/2})$, $j \in \{i+1/2, i-1/2\}$ and $P_{i+1/2}$ and $P_{i-1/2}$ correspond to pressure from right and left neighbor cells, respectively. Here, we defined the cell density at cell i as $\rho_i = 1/(x_{i+1/2} - x_{i-1/2})$, where $i+1/2$ represents the middle point index between cell i and cell $i+1$. In the same way, the natural cell density at cell i is defined by inverse of sum of natural radius of neighboring cells as $\rho_i^\infty = 1/(R_{i+1/2} + R_{i-1/2})$. These definitions lead to $P_j = 1/\rho_j^\infty - 1/\rho_j$. Thus, the equation (2) becomes

$$\frac{dv_j}{dt} = -\mu\left(ERK_j\right)v_j - k\frac{1}{\rho_j}\frac{\partial P}{\partial x}\bigg|_j + \eta\left(x_{j+1/2} - x_{j-1/2}\right) \times \left(\frac{\frac{1}{\rho_{j+1/2}}\frac{\partial v}{\partial x}\bigg|_{j+1/2} - \frac{1}{\rho_{j-1/2}}\frac{\partial v}{\partial x}\bigg|_{j-1/2}}{x_{j+1/2} - x_{j-1/2}}\right), \quad (12)$$

where $\partial P/\partial x|_i = (P_{i+1/2} - P_{i-1/2})/(x_{i+1/2} - x_{i-1/2})$, $\partial v/\partial x|_j = (v_{j+1/2} - v_{j-1/2})/(x_{j+1/2} - x_{j-1/2})$ and $j \in \{i+1/2, i-1/2\}$. According to continuous approximation, i.e. $\lim_{(x_{j+1/2} - x_{j-1/2}) \to 0}$, this equation is transformed into

$$\frac{Dv}{Dt} = -\mu(ERK)v - k\frac{1}{\rho}\frac{\partial P}{\partial x} + \eta\frac{1}{\rho}\frac{\partial}{\partial x}\left(\frac{1}{\rho}\frac{\partial v}{\partial x}\right) = -\mu(ERK)v - k\frac{1}{\rho}\frac{\partial P}{\partial x} + \eta\left(\frac{1}{\rho^2}\frac{\partial^2 v}{\partial x^2} - \frac{1}{\rho^3}\frac{\partial \rho}{\partial x}\frac{\partial v}{\partial x}\right), \quad (13)$$

where v indicates continuous function of x and t as $v(x, t)$, $P = 1/\rho^\infty(\mathrm{ERK}) - 1/\rho$, $\rho^\infty(ERK) = 1/2R(ERK)$ and $Dv/Dt = \partial v/\partial t + v\, \partial v/\partial x$. Note that Dv/Dt indicates Lagrange description of velocity, representing temporal derivative of migration velocity of tracking cells. P is defined by $P(x, t) = 1/\rho^\infty(x, t) - 1/\rho(x, t)$, where $\rho^\infty(x, t) = 1/2R(ERK(x, t))$. Here, we considered $R(ERK) = Ro\,(1 + \alpha ERK)$ as in the particle-based model, which leads to equation (5).

To obtain continuum dynamics of cell density, we consider temporal derivative of $\rho_{i+1/2}$ referring the definition $\rho_i = 1/(x_{i+1/2} - x_{i-1/2})$ as

$$\frac{d\rho_i}{dt} = \frac{d}{dt}\frac{1}{x_{i+1/2} - x_{i+1/2}} = -\frac{1}{x_{i+1/2} - x_{i+1/2}}\left(\frac{v_{i+1/2} - v_{i+1/2}}{x_{i+1/2} - x_{i+1/2}}\right). \quad (14)$$

In the same manner in the case of velocity above, this equation changes to

$$\frac{d\rho_i}{dt} = -\rho_i\frac{\partial v}{\partial x}\bigg|_i. \quad (15)$$

Again, continuum approximation leads to temporal derivative of density in Lagrange description:

$$\frac{D\rho}{Dt} = -\rho\frac{\partial \rho}{\partial x}. \quad (16)$$

This equation can be changed in Euler description as

$$\frac{\partial \rho}{\partial t} = -\frac{\partial}{\partial x}(\rho v). \quad (17)$$

This equation is well known as 'continuity equation', resulting from the law of mass conservation in continuum dynamics. Because it is naturally derived, our continuum approximation was accurate.

Numerical simulation for the particle-based model

Numerical simulations for the particle-based ODE model were conducted by Runge-Kutta method with fourth order accuracy. The initial positions of the particles were equally spaced on x-axis with 1.0 as the space from one cell to its neighbor.

Numerical simulation for the continuum model

***Discretization of the continuum model*:** For numerical simulations, the continuum PDE model in Euler description were discretized with local Lax-Friedrichs flux (Shu, 2009). PDEs were generally expressed by

$$\frac{\partial u}{\partial t} + \frac{\partial f(u)}{\partial x} = g(x,t), \tag{18}$$

where $u \in \{\rho(x,t), v(x,t)\}$, $f(u)$ indicates flux, e.g., $f(\rho)=\rho v$ for cell density and $f(v)=v^2/2$ for cell density, and $g(t)$ indicates reaction terms, e.g., $g(t)=0$ for cell density and $g(t)$ equals to right-hand of equation (9). This PDE can be discretized in space and time as

$$u_j^{\tau+1} = u_j^{\tau} + \frac{\Delta t}{\Delta x}\left(f_{j+1/2}^{\tau} - f_{j-1/2}^{\tau}\right) + g_j^{\tau}\Delta t, \tag{19}$$

where j and τ denote indices of discretized space and time, respectively; $j\pm1/2$ corresponds mid positions between j and $j\pm1$; Δx and $\Delta\tau$ indicate the discretized intervals of space and time, respectively; s_j^{τ} indicates value at time $\tau\Delta t$ and position $j\Delta x$, and ($s \in \{u, f, g\}$); u_j^{τ} represents the spatial average of $u(x)$ at space j as

$$u_j^{\tau} = \frac{1}{\Delta x}\int_{x_{j-1/2}}^{x_{j+1/2}} u(x,\tau)dx. \tag{20}$$

Since $f_{j\pm1/2}$ indicates flux at the mid positions between j and $j\pm1$, this equation satisfies conservation of u. Here, we considered the discontinuity at $j\pm1/2$ such that $\lim_{\delta\to+0} u((j\pm1/2)\Delta x+\delta,\tau\Delta t) = {u_{j\pm1/2}^{\tau}}^{R}$ and $\lim_{\delta\to-0} u((j\pm1/2)\Delta x+\delta,\tau\Delta t) = {u_{j\pm1/2}^{\tau}}^{L}$. Fluxes at $j\pm1/2$ were defined by Lax-Friedrichs flux as

$$f_{j\pm1/2}^{\tau} = \frac{1}{2}\left\{f\left({u_{j\pm1/2}^{\tau}}^{R}\right) + f\left({u_{j\pm1/2}^{\tau}}^{L}\right)\right\} - \frac{\gamma}{2}\left({u_{j\pm1/2}^{\tau}}^{R} - {u_{j\pm1/2}^{\tau}}^{L}\right), \tag{21}$$

where $\gamma=\max_x|f(u(x))|$. The first term represents the average flux, whereas the second term is artificial diffusion for avoiding numerical stability. ${u_{j+1/2}}^{L}$ and ${u_{j+1/2}}^{R}$ in equation (21) were calculated by weighted essentially non-oscillatory (WENO) scheme (Cockburn et al., 2006; Shu, 2009) described below.

***The WENO scheme*:** We used the fifth-order WENO scheme to compute ${u_{j+1/2}}^{L}$ and ${u_{j+1/2}}^{R}$ from values of u at the grid points in the stencils $S^L=\{x_{j-2}, x_{j-1}, x_j, x_{j+1}, x_{j+2}\}$ and $S^R=\{x_{j-1}, x_j, x_{j+1}, x_{j+2}, x_{j+3}\}$, respectively. The WENO scheme is a local interpolation method with taking account for discontinuity of $u(x)$. Because u_j represents spatial average of $u(x)$ over the interval $[x_{j-1/2}, x_{j+1/2}]$, we just only know its integral as

$$U_{j+1/2} = \int_{x_0}^{x_{j+1/2}} u(x)dx = \Delta x\sum_{l=0}^{j} u_l\,. \tag{22}$$

In the WENO reconstruction procedure (Cockburn et al., 2006), values of U were interpolated by the three different stencils of $S^{(1)}=\{x_{j-5/2}, x_{j-3/2}, x_{j-1/2}, x_{j+1/2}\}$, $S^{(2)}=\{x_{j-3/2}, x_{j-1/2}, x_{j+1/2}, x_{j+3/2}\}$ and $S^{(3)}=\{x_{j-1/2}, x_{j+1/2}, x_{j+3/2}, x_{j+5/2}\}$ as third-order polynomials, $P^{(1)}(x)$, $P^{(2)}(x)$ and $P^{(3)}(x)$, respectively. Then, values of u were

reconstructed by second-order polynomials as $p^{(n)}(x) = dP^{(n)}(x)/dx$, and $u_{j+1/2}$ is approximated to values of $p^{(n)}(x_{j+1/2})$ as

$$u_{j+1/2}^{(1)} = \frac{1}{3}u_{j-2} - \frac{7}{6}u_{j-1} + \frac{11}{6}u_j, \tag{23}$$

$$u_{j+1/2}^{(2)} = -\frac{1}{6}u_{j-1} + \frac{5}{6}u_j + \frac{1}{3}u_{j+1}, \tag{24}$$

$$u_{j+1/2}^{(3)} = \frac{1}{3}u_j + \frac{5}{6}u_{j+1} - \frac{1}{6}u_{j+2}. \tag{25}$$

Then, ${u_{j+1/2}}^L$ was approximated by a convex combination of the three reconstructed $u_{j+1/2}$ as

$${u_{j+1/2}}^L = w_1 u_{j+1/2}^{(1)} + w_2 u_{j+1/2}^{(2)} + w_3 u_{j+1/2}^{(3)}, \tag{26}$$

where $\sum_n w_n = 1$ and these weights are modulated in a discontinuity-dependent manner as

$$w_n = \frac{\widehat{w}_n}{\sum_k \widehat{w}_k}, \tag{27}$$

with

$$\widehat{w}_n = \frac{\lambda_n}{(\varepsilon + s_n)^2}, \tag{28}$$

where λ_1=1/10, λ_2=6/10, λ_3=3/10 and ε=10^{-6}. s_n is smoothness indicator of $p^{(n)}(x)$ defined by

$$s_n = \sum_l^m \Delta x^{2l-1} \int_{x_{j-1/2}}^{x_{j+1/2}} \left(\frac{d^l}{dx^l} p^{(n)}(x) \right)^2 dx\,, \tag{29}$$

where m is the polynomial degree of $p^{(n)}(x)$ (in this case, m=2). The smoothness indicators were formulated by

$$s_1 = \frac{13}{12}\left(u_j - 2u_{j+1} + u_{j+2}\right)^2 + \frac{1}{4}\left(3u_j - 4u_{j+1} + u_{j+2}\right), \tag{30}$$

$$s_2 = \frac{13}{12}\left(u_{j-1} - 2u_j + u_{j+1}\right)^2 + \frac{1}{4}\left(u_{j-1} - u_{j+1}\right), \tag{31}$$

$$s_3 = \frac{13}{12}\left(u_{j-2} - 2u_{j-1} + 3u_j\right)^2 + \frac{1}{4}\left(u_{j-2} - 4u_{j-1} + 3u_j\right). \tag{32}$$

Note that if $u(x)$ is smooth from x_{j-1} to x_{j+3} (i.e., s_1=s_2=s_3), ${u_{j+1/2}}^L$ becomes exactly the same as a polynomial of degree at most four on large stencil S. Similarly, ${u_{j+1/2}}^R$ can be calculated on stencil S^R, but in a mirror symmetric manner with respect to x_j of the above procedure.

***Numerical simulation in Euler description*:** The equation (18) can be written as a method-of-line ODEs system

$$\frac{du_j}{dt} = \frac{1}{\Delta x}\left(f_{j+1/2} - f_{j-1/2}\right) + g_j \equiv L(\boldsymbol{u_j}), \tag{33}$$

where $\boldsymbol{u}_j$ ={u_{j-2}, u_{j-1}, u_j, u_{j+1}, u_{j+2}, u_{j+3}}. These ODEs were temporally integrated by the total variation diminishing (TVD) Runge-Kutta method with third order accuracy (Shu, 2009) as

$$u_j^{(1)} = u_j^\tau + L(\boldsymbol{u}_j^\tau)\Delta t, \tag{34}$$

$$u_j^{(2)} = \frac{3}{4}u_j^\tau + \frac{1}{4}u_j^{(1)} + \frac{1}{4}L\left(\boldsymbol{u}_j^{(1)}\right)\Delta t, \tag{35}$$

$$u_j^{\tau+1} = \frac{1}{3}u_j^\tau + \frac{2}{3}u_j^{(2)} + \frac{2}{3}L\left(\boldsymbol{u}_j^{(2)}\right)\Delta t, \tag{36}$$

where $\boldsymbol{u}_j^{(k)}$={${u_{j-2}}^{(k)}$, ${u_{j-1}}^{(k)}$, $u_j^{(k)}$, ${u_{j+1}}^{(k)}$, ${u_{j+2}}^{(k)}$, ${u_{j+3}}^{(k)}$}.

***Numerical simulation in Lagrange description*:** After getting the field value $v(x(x_0,t),t)$, Lagrange-described value $x(x_0,T)$ at time T is calculated by

$$\frac{dx}{dt} = v(x,t). \tag{37}$$

Referring the field $v(x,t)$. The calculations were conducted on Runge-Kutta methods with forth order accuracy. Initial positions of particles on the tissue were determined as the same initial positions as those in particle model simulations.

Acknowledgement

We thank Dr. Michiyuki Matsuda in Kyoto University for helpful discussion. This study was mainly supported by the Cooperative Study Program of Exploratory Research Center on Life and Living Systems (ExCELLS) (ExCELLS program No.18-201). It was also supported by JSPS KAKENHI Grants (16K16147 (H.N.), 18H02444, 19H05798 (K.A.), 19H05438, 19K16207 (Y.K.)), by JST CREST Grant JPMJCR1654 (K.A.).

References

Aoki, K., Kondo, Y., Naoki, H., Hiratsuka, T., Itoh, R.E., and Matsuda, M. (2017). Propagating Wave of ERK Activation Orients Collective Cell Migration. Dev Cell *43*, 305–31700000.

Avvisato, C.L., Yang, X., Shah, S., Hoxter, B., Li, W., Gaynor, R., Pestell, R., Tozeren, A., and Byers, S.W. (2007). Mechanical force modulates global gene expression and β-catenin signaling in colon cancer cells. J Cell Sci *120*, 2672–2682.

Brodland, G. (2003). Do lamellipodia have the mechanical capacity to drive convergent extension? Int J Dev Biol *50*, 151–155.

Cockburn, B., Shu, C.-W., Johnson, C., and Tadmor, E. (2006). Advanced Numerical Approximation of Nonlinear Hyperbolic Equations, Lectures given at the 2nd Session of the Centro Internazionale Matematico Estivo (C.I.M.E.) held in Cetraro, Italy, June 23–28, 1997. 325–432.

Fozard, J., Byrne, H., Jensen, O., and King, J. (2009). Continuum approximations of individual-based models for epithelial monolayers. Math Medicine Biology J Ima *27*, 39–74.

Friedl, P., and Gilmour, D. (2009). Collective cell migration in morphogenesis, regeneration and cancer. Nat Rev Mol Cell Bio *10*, 445–457.

cois Graner, F., Glazier, J., cois Graner, F., and Glazier, J. (1992). Graner et al-1992-Phys Rev Lett.pdf. Phys Rev Lett.

Hiratsuka, T., Fujita, Y., Naoki, H., Aoki, K., Kamioka, Y., and Matsuda, M. (2015). Intercellular propagation of extracellular signal-regulated kinase activation revealed by in vivo imaging of mouse skin. Elife *4*, e05178.

Honda, H. (1983). Geometrical Models for Cells in Tissues. Int Rev Cytol *81*, 191–248.

Huang, C., Jacobson, K., and of cell science, S. (2004). MAP kinases and cell migration. J Cell Sci.

Ishihara, S., Marcq, P., and Sugimura, K. From cells to tissue: A continuum model of epithelial mechanics. Phys Rev E *96*, 22418.

Kamioka, Y., Sumiyama, K., Mizuno, R., Sakai, Y., Hirata, E., Kiyokawa, E., and Matsuda, M. (2012). Live Imaging of Protein Kinase Activities in Transgenic Mice Expressing FRET Biosensors. Cell Struct Funct *37*, 65–73.

Komatsu, N., Aoki, K., Yamada, M., Yukinaga, H., Fujita, Y., Kamioka, Y., and Matsuda, M. (2011). Development of an optimized backbone of FRET biosensors for kinases and GTPases. Mol Biol Cell *22*, 4647–4656.

Mizuno, R., Kamioka, Y., Kabashima, K., Imajo, M., Sumiyama, K., Nakasho, E., Ito, T., Hamazaki, Y., Okuchi, Y., Sakai, Y., et al. (2014). In vivo imaging reveals PKA regulation of ERK activity during neutrophil recruitment to inflamed intestines. J Exp Medicine *211*, 1123–1136.

Murisic, N., Hakim, V., Kevrekidis, I.G., Shvartsman, S.Y., and Audoly, B. (2015). From Discrete to Continuum Models of Three-Dimensional Deformations in Epithelial Sheets. Biophys J *109*, 154–163.

Nonomura, M. (2012). Study on Multicellular Systems Using a Phase Field Model. Plos One *7*, e33501.

Pascalis, C., and Etienne-Manneville, S. (2017). Single and collective cell migration: the mechanics of adhesions. Mol Biol Cell *28*, 1833–1846.

Shu, C.-W. (2009). High Order Weighted Essentially Nonoscillatory Schemes for Convection Dominated Problems. Siam Rev *51*, 82–126.

Turner, S. (2005). Using cell potential energy to model the dynamics of adhesive biological cells. Phys Rev E *71*, 041903.

Yamao, M., Naoki, H., and Ishii, S. (2011). Multi-Cellular Logistics of Collective Cell Migration. Plos One *6*, e27950.

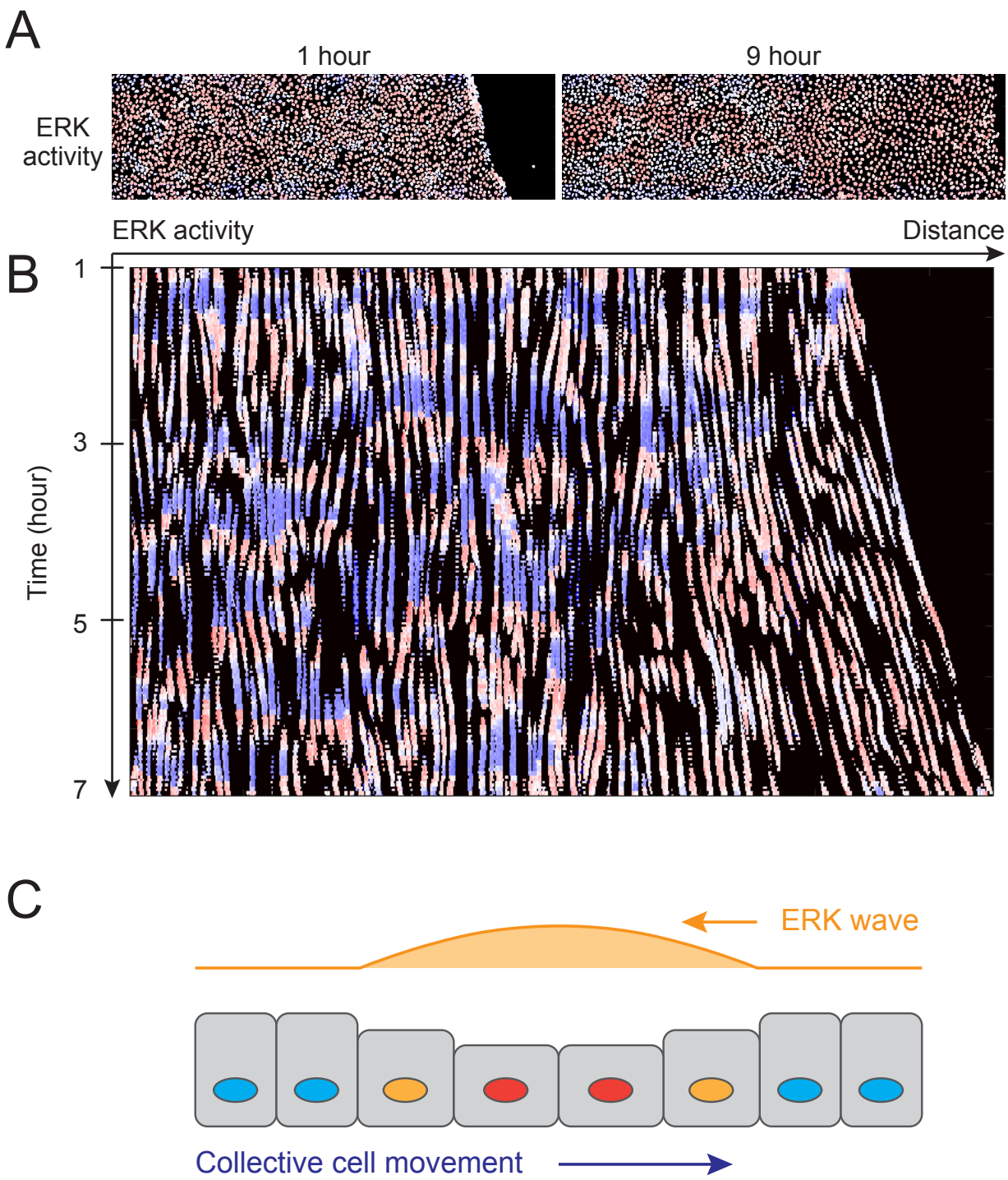

Figure 1: Live imaging of ERK-induced collective cell migration

A. Visualization of ERK activity during the wound-healing in epithelial sheet of MDCK cells expressing the FRET-based biosensor of ERK. Snapshots are presented at 1 hr (left) and 9 hr (right) after scratching. Red and blue colors indicate high and low ERK activity, respectively.

B. A kymograph of ERK activity images of cells that locate on a line of interest indicated by white line in (a).

C. A schematic representation of ERK-mediated collective cell migration. Cells migrate toward the opposite direction of the ERK wave. The cellular volume and mobility are increased by the ERK activation.

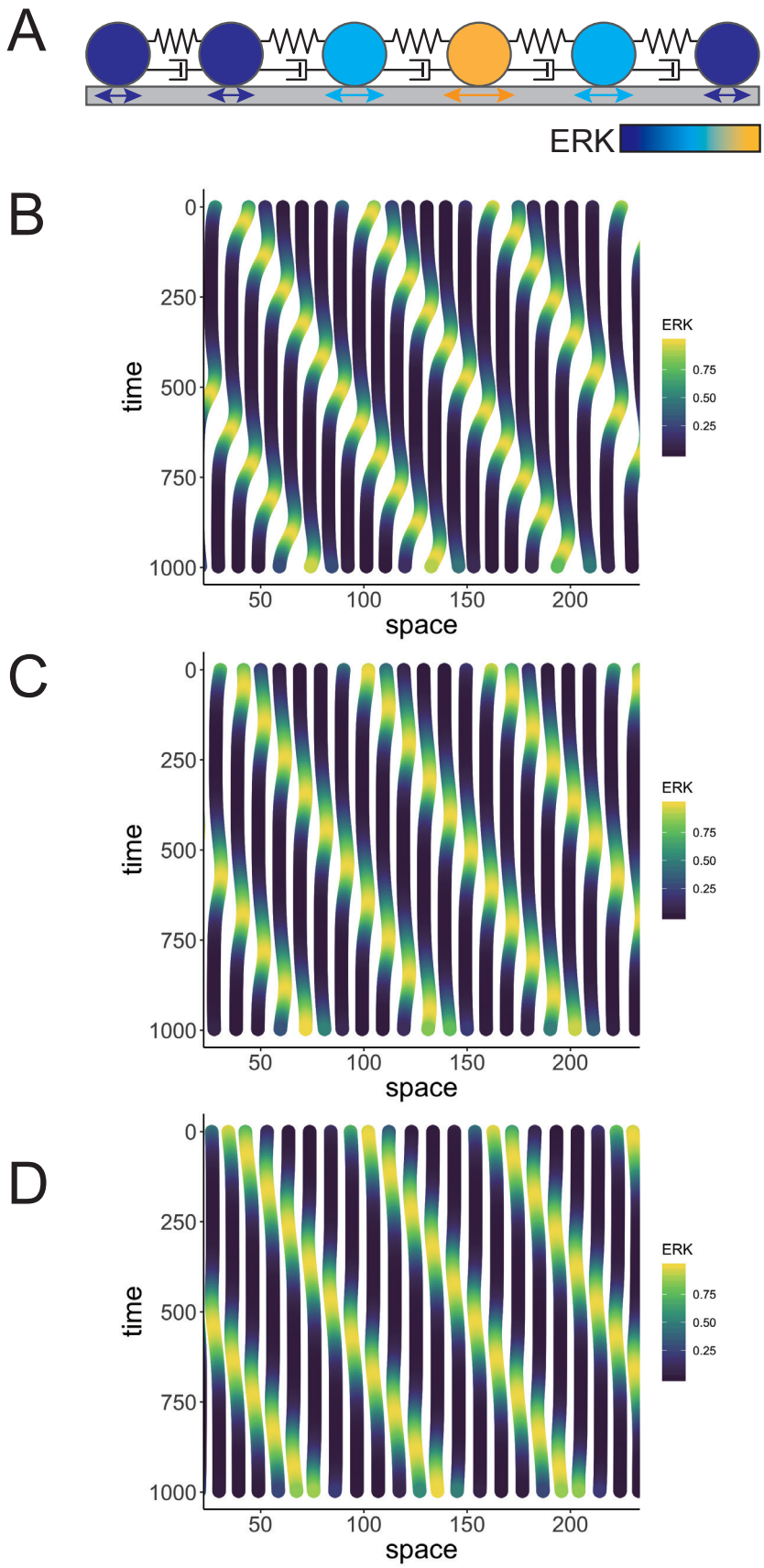

Figure 2: Particle-based model

A. Graphical representation of the particle-based model. The centers of cells are illustrated by particles, and these are connected with neighboring cells by springs and dampers representing elasticity and viscosity of cytoplasm, respectively.

B-D. Simulations of ERK-induced cell migration. Each line indicates cellular trajectory with color representing ERK activity. Parameters in Table 1 were used unless stated. In (B), cells migrate toward the opposite direction of the ERK waves (α=1.5 and β=2.5). In (C), cells show back-and-forth movement during the ERK waves without net displacement (α =1.5 and β=0). In (D), cell migrate toward the same direction of the ERK waves (α=−0.4 andβ=2.5).

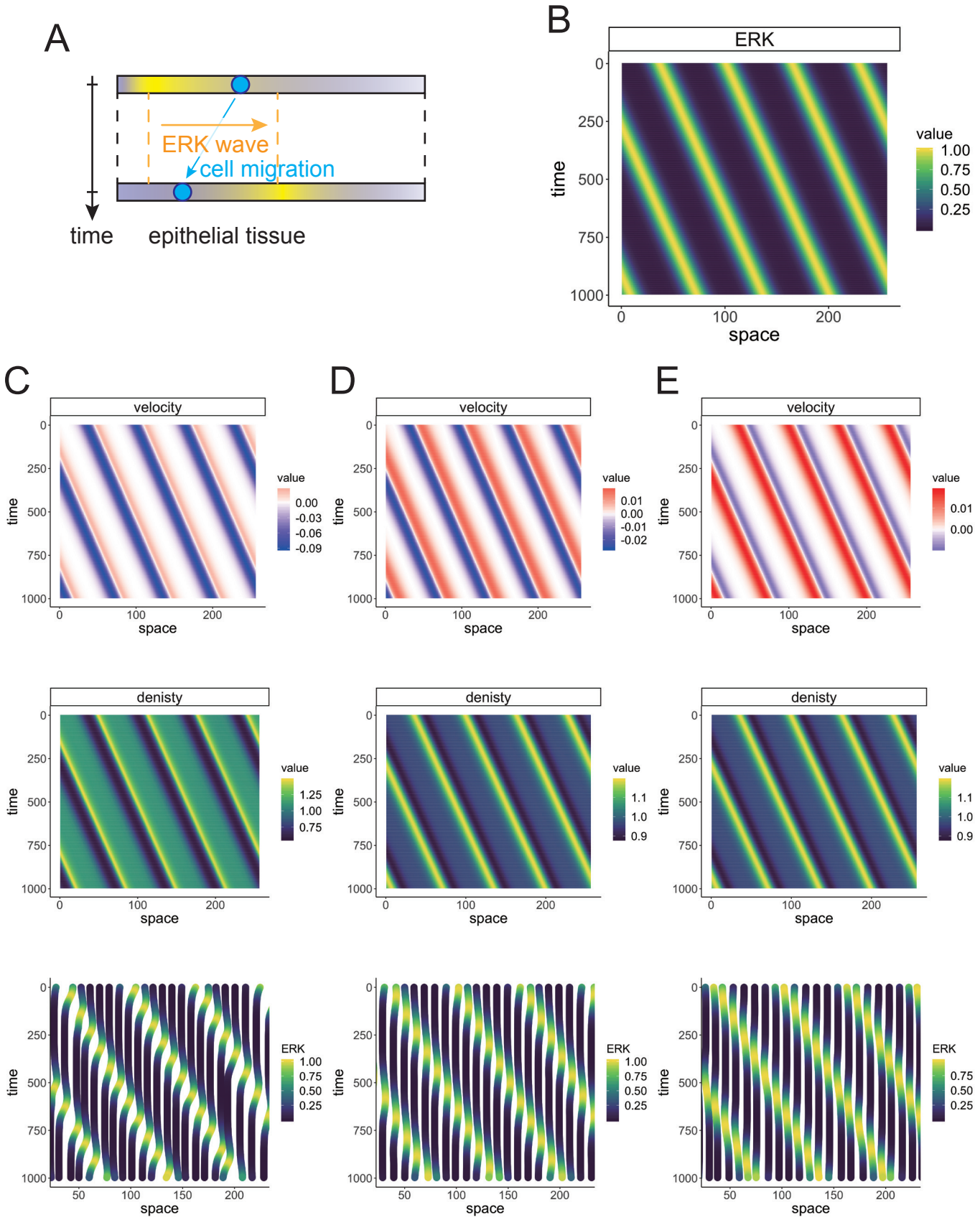

Figure 3: Continuum model

A. A schematic representation of ERK-mediated tissue dynamics (shown as planes) and cell migration trajectories (shown as blue points and lines). Colors of the tissue indicates an ERK travelling wave.

B. ERK travelling waves applied in simulations.

C-E. Simulation results of velocity (upper panel), density (middle panel), and trajectories of the cells (lower panel). Parameters used for the simulations in (C), (D) and (E) are the same as figure 2B, C and D, respectively.

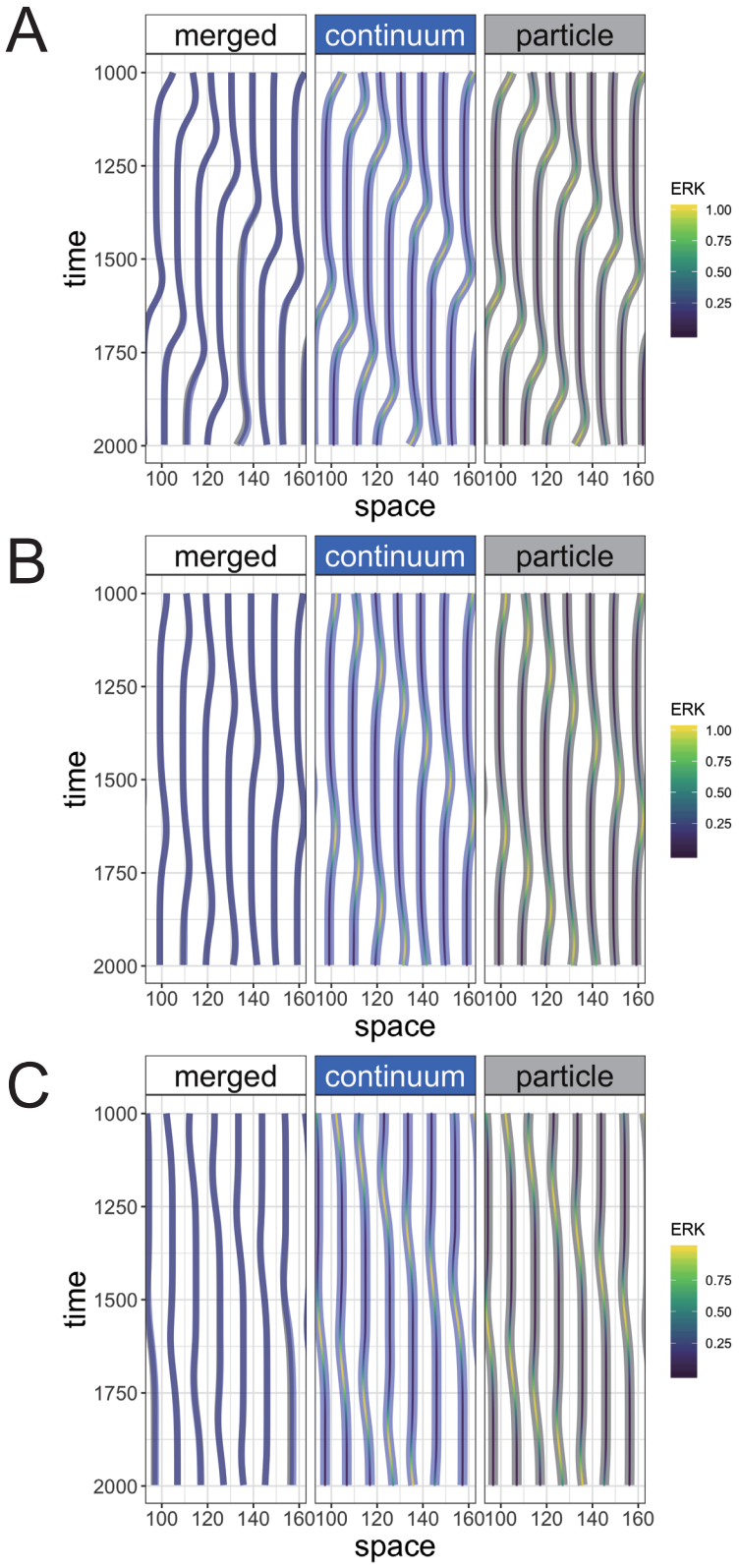

Figure 4: Comparison between the particle-based and continuum models
Comparisons between the migration trajectories simulated by two models with the same parameter values. In left and right panels, shaded blue and gray lines indicate trajectories simulated by the continuum and particle-based models, respectively, and color of inside lines indicates ERK activity. In middle panels, shaded blue and gray lines were merged for comparison. Parameters used in (A), (B) and (C) are the same as figure 2B, C and D, respectively.

Table1: List of parameter value

variables	**Fig2B** **Fig3C-E left** **Fig4A**	**Fig2C** **Fig3C-E middle** **Fig4B**	**Fig2D** **Fig3C-E right** **Fig4C**
mu0	10	10	10
alpha	1.5	1.5	-0.4
beta	2.5	0	2.5
k0	2	2	2
R0	0.5	0.5	0.5
eta	0.08	0.08	0.08